Article

Low Temperature Step Annealing Synthesis of the Ti$_2$AlN MAX Phase to Fabricate MXene Quantum Dots

Sophia Akhtar [†], Shrawan Roy [†], Trang Thu Tran, Jaspal Singh, Anir S. Sharbirin and Jeongyong Kim *

Department of Energy Science, Sungkyunkwan University, Suwon 16419, Korea; sophia77@skku.edu (S.A.); shrawanroy@skku.edu (S.R.); t.tran@skku.edu (T.T.T.); jaspal.2125@skku.edu (J.S.); anirsyahmi@skku.edu (A.S.S.)
* Correspondence: j.kim@skku.edu
† These authors contributed equally to this work.

Abstract: We present the synthesis of the Ti$_2$AlN MAX phase using two-step annealing at temperatures of 600 °C and 1100 °C, the lowest synthesis temperatures reported so far. After the successful synthesis of the Ti$_2$AlN MAX phase, two-dimensional Ti$_2$N MXene was prepared through wet chemical etching and further fragmented into light emitting MXene quantum dots (MQDs) with a size of 3.2 nm by hydrothermal method. Our MQDs displayed a 6.9% quantum yield at a 310 nm wavelength of excitation, suggesting promising nanophotonic applications.

1. Introduction

The MAX phases are a family of advanced ceramic materials comprised of hexagonal layered transition metal carbides, nitrides, and carbonitrides, which have been explored for more than a decade [1,2]. Generally, the MAX phases are denoted as $M_{n+1}AX_n$, where M is an early transition metal (Sc, V, Ti, etc.), A is an element from group 13–16, and X is either nitrogen or carbon with a stoichiometry of n = 1, 2, 3 [3]. The crystal structure of the MAX phases contains a hexagonal lattice with space group P63/mmc in which adjacent $M_{n+1}X_n$ octahedral sites are interleaved with atomic monolayers of A atoms [4]. The MAX phases have been given considerable attention owing to their unique and interesting combination of metallic as well as ceramic properties [5]. Because of their metallic character, MAX phases exhibit high thermal and electrical conductivity along with thermal shock resistance. The ceramic property of the MAX phase material enables it to possess remarkable oxidation and corrosion resistance at high temperature operations [6]. Owing to their fascinating properties, more than 155 MAX phases have currently been synthesized [5].

Among the numerous MAX phases, ternary MAX phases based on the Ti-Al-N system are more demanding because of their oxidation resistance at high temperatures [4,7]. The synthesis of bulk Ti$_2$AlN in a single phase is difficult owing to its strong chemical bonding [8] and low stability [9], which provides an opportunity to investigate and explore different methods for the synthesis of Ti$_2$AlN MAX phase. Thus, the bulk Ti$_2$AlN MAX phase had been synthesized via multiple methods. The spectrum of these methods is broad and includes high-temperature synthesis [10–13], molten salt synthesis [14–16], hot isostatic pressing (HIP) [17–19], hot pressing (HP) [20–22], field assisted sintering technology (FAST) [6], spark plasma sintering (SPS) [4,6,23,24], ultra-high vacuum (UHV) deposition chamber reactive magnetron sputtering [1], microwave sintering [2], and shock-activated reaction synthesis [25].

As MAX phases possess both ceramic and metallic properties, their synthesis at low temperatures is difficult. Previous studies have reported the presence of significant amounts of impurities such as TiN, Ti$_3$Al, TiAl, AlN, Al$_2$Ti, and Al$_3$Ti [2,15,21] during the synthesis of MAX phases at temperatures lower than 1400–1500 °C. Thus, most of the previous methods for synthesizing Ti$_2$AlN require a high temperature, which entails

much more investment and is not easily available in common laboratories. One of the main hindrances to synthesizing MAX phase materials is the use of an expensive apparatus because commonly available furnaces have temperature limitations and can only be used at temperatures of 1100–1200 °C or less. Thus, there is always a strong demand for new, easily accessible, simple, and low-cost methods for the synthesis of Ti_2AlN MAX phases with better crystal quality and lower temperature (~1100 °C) systems compared to the methods described in previous works.

The ternary MAX phase can be easily converted into two-dimensional (2D) layered MXene sheets using a simple wet chemical etching process [10] and can be further reduced to zero-dimensional MXene quantum dots (MQDs) [26]. Similar to 2D materials such as graphene [27] and transition metal dichalcogenide (TMD)-based quantum dots [28–30], MQDs have become a center of interest for many researchers because of their excellent properties, such as good light emission [31,32], selective metal ion sensing [33–36], non-toxicity [26,37,38], biocompatibility [26], hydrophilicity [35], and functionalization [39,40]. Owing to their interesting optical properties, they can be used as crucial materials in optical sensors [41,42], bio-imaging [34], optical modulator [43] etc. Comparatively, carbide MQDs [44,45] derived from the MAX phase containing a carbide group such as V_2AlC [46], Nb_2AlC [33], and Ti_3AlC_2 [39] have been studied more than nitride MQDs [10,26]; thus, the exploration and broad study of the properties and applications of nitride based MQDs are necessary.

In this study, we introduce a new step annealing method to synthesize the Ti_2AlN MAX phase at a relatively lower temperature compared to previously reported methods and soaking times. This method includes a two-step annealing process at 600 °C and 1100 °C, which is a comparatively lower temperature than previous techniques, and yields a better quality Ti_2AlN MAX phase with completely removed unavoidable impurities such as TiN, which were mostly obtained during synthesis at low temperatures. The as-synthesized Ti_2AlN MAX phase was etched out using wet chemical etching to prepare its corresponding 2D MXene sheets, which were further decomposed into light emitting MQDs by a hydrothermal process. The formation of the Ti_2AlN samples, Ti_2N Mxene sheets, and MQDs was further confirmed and comprehensively visualized and studied by X-ray diffraction (XRD), field emission scanning electron microscopy (FE-SEM), high-resolution transmission electron microscopy (HR-TEM), Raman spectroscopy, photoluminescence (PL) spectroscopy, X-ray photon spectroscopy (XPS) and Ultraviolet-visible (UV-vis) spectroscopy.

2. Materials and Methods

2.1. Synthesis of Ti₂AlN MAX Phase via Step Annealing Method

Commercial powders of elemental titanium (Ti, −325 mesh, Sigma Aldrich, St. Louis, MO, USA), aluminum (Al, −325 mesh, Sigma Aldrich), and aluminum nitride (AlN, Sigma Aldrich) were used as the initial precursors for the preparation of the Ti_2AlN MAX phase. All powders were used as received without further treatment.

The precursor ratio of starting powder mixtures of 2Ti + 0.8Al + AlN was used. Since Al could evaporate and dissociate during the processing, which inhibits the single-phase synthesis of Ti_2AlN [47], an excess amount of Al was introduced to compensate for the Al loss. Ti, Al, and AlN powders were weighed on a precision scale (0.0001 g) at a molar ratio of 2:0.8:1. Powder mixtures and zirconia balls were sealed in a dry environment with a dew point of nearly −55 °C to avoid the introduction of moisture during the milling process. The powders were thoroughly ball-milled in a stainless-steel vessel by using a Fritsch Pulverisette planetary mill [11]. The powders were finely milled using a unique set of milling conditions in two steps, using a powder-to-ball ratio of 1:4. In step 1, a low rpm of 270 was used, and the powders were milled for 6 h, whereas in step 2, a high rpm of 400 was used for another 6 h of milling. These steps in the milling process enabled the thorough mixing of the precursors. The high-rpm step plays a significant role in the mechanical activation [48] of the mixed powders. Mechanical activation helps the disintegration of constituents to yield smaller sized powders while increasing the active

surface area. Consequently, decreasing the time and the temperature of synthesis are desirable for Ti_2AlN synthesis. The mixed powders were placed in a stainless-steel die and compacted into 13 mm diameter pellets by applying a uniaxial pressure of 4 MPa.

For this particular step annealing synthesis method, the pellets were placed in an alumina crucible and placed in a double-tube furnace, where a constant flow of argon gas was maintained throughout the thermal annealing process. This method includes two different steps, involving different heating rates and temperatures. First, a heating rate of 5 °C/min was used to reach 600 °C with a soaking time of 1 h. Second, a relatively high heating rate of 20 °C/min was used to reach 1100 °C from 600 °C, and the sample was soaked for 3 h at that temperature. After completion of the synthesis process, the pellets were naturally cooled to room temperature and ground with an agate mortar pestle to obtain Ti_2AlN MAX phase powder.

2.2. Synthesis of MXene and MQDs

Ti_2N MXene was prepared by chemical etching of the Al layers from the Ti_2AlN MAX phase by following a previously reported method [10]. During the chemical etching process, the etchant was prepared by dissolving 6 g KF in 5M HCl then 1 g of the MAX phase was added to 20 mL of the prepared etchant solution and kept undistributed for 3 h. Subsequently, the etching solution with the MAX phase was bath-sonicated for 1 h at 40 °C to accelerate intercalation, which further assisted the exfoliation process. Subsequently, the solution was centrifuged and washed with DI water until the pH became neutral. Finally, the MXene sheets were filtered and dried overnight at 40 °C. The yield of MXene formation was found to be approximately 70%, which is comparable to the previously reported yield [10].

MQDs were synthesized using a hydrothermal method followed by centrifugation [35]. The obtained Ti_2N MXene after Al etching from Ti_2AlN MAX was dispersed in DI water, and the pH of the solution was adjusted to 10 by the addition of ammonium hydroxide (NH_4OH) solution. This solution was poured into a Teflon container that was placed in an autoclave. The autoclave was then placed in an oven at 100 °C for 6 h and cooled to room temperature. After cooling, the solution was centrifuged (10,000 rpm) for 20 min, and the MQDs were collected as dispersed in the supernatant. The supernatant was carefully separated and stored in a refrigerator for frequent use for further characterization.

2.3. XRD, PL, Raman Spectroscopy, UV-Vis Absorption, PL Excitation (PLE), Quantum Yield (QY), FE-SEM, XPS and HR-TEM Measurements

The XRD patterns of the Ti_2AlN MAX phase and corresponding Ti_2N MXene were recorded using a Bruker AXS diffractometer (D2 PHASER A26-X1-A2B0B2A Karlsruhe, Germany) at room temperature. Raman spectra were recorded using a WITec confocal microscope system (Alpha-300 SR, WITec GmbH, Ulm, Germany) equipped with a 100× objective lens (N.A. = 0.9) with an excitation wavelength of 532 nm. UV-Vis absorption spectra of the Ti_2N MQDs were recorded in deionized water (Optizen UV-Vis spectrometer). PL and PLE spectra were measured using a Cary Eclipse spectrometer. The quantum yield of the Rhodamine 6G (R6G) solution was measured using a Quantaurus-QY, Hamamatsu Photonics spectrometer. FE-SEM (JSM-7600F, JEOL Corp., Tokyo, Japan) images of the Ti_2AlN MAX phase and Ti_2N MXene were captured at field voltages ranging from 5 kV to 10 kV. XPS of MQDs was recorded using X-ray photon spectrometer (ESCALAB250). The HR-TEM (JEM-3010, JEOL Corp.) images of the MQDs were obtained at 300 kV.

3. Results and Discussion

The schematic diagram in Figure 1 illustrates a brief process of the new step annealing method for synthesizing the (211) Ti_2AlN MAX phase beginning from the precursors. This is comprehensively explained in the experimental section. Generally, MAX phase ceramics are synthesized at high temperatures [49], and it is very difficult to obtain relative purity at lower temperatures. As illustrated in the schematic diagram, the 3D ceramic MAX phase of Ti_2AlN was prepared using a unique step annealing method in an argon environment

after pelletizing the precursors. In this particular method, a temperature soaking step at 600 °C for 1 h was maintained in step 1 because the melting point of Al is relatively low compared to other precursors, that is, 660 °C, which causes inevitable weight loss at higher temperatures [47]. The desorption of Al occurs at temperatures greater than 600 °C because of its high vapor pressure [50]. The absence of Al at high temperatures can change the composition of the reaction system. To overcome this phenomenon, the precursor ratio was initially adjusted and excess of Al was added to the composition. The increased formation of TiN phase impurities occurs in the temperature range of 900 °C to 1000 °C [50]. Therefore, from step 1 to step 2 of annealing, a higher step rate of 20° min^{-1} was used to inhibit TiN formation. In step 2, the temperature soaking step was maintained at 1100 °C for 3 h to complete the MAX phase synthesis.

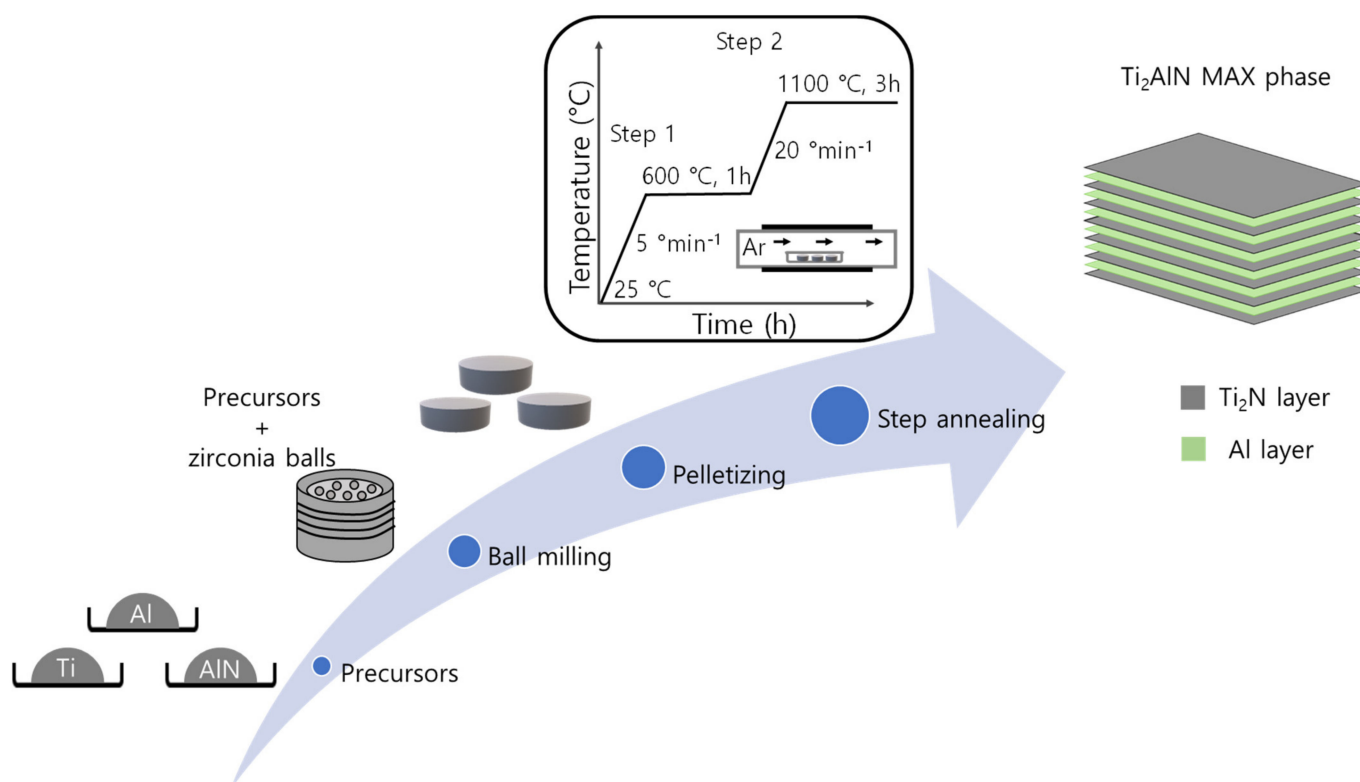**Figure 1.** Schematic illustration of Ti$_2$AlN MAX phase synthesis by step annealing method.

The XRD pattern of the as-synthesized Ti$_2$AlN MAX phase was recorded in the range of 10°$-$80° within 2θ angle using CuKα radiation (λ = 1.54 Å) with a step size of 0.01°, as shown in Figure 2a. The Ti$_2$AlN MAX phase synthesized by the step annealing method with the optimized precursor ratio, indicated by the black profile in Figure 2a, contains most of the diffraction peaks of Ti$_2$AlN and small amounts of TiAl with a peak position at 38.9° as an impurity. The prominent peaks in the pattern were observed at 12.9°, 34.6°, 35.2°, 39.6°, 40.0°, 43.9°, 53.6°, 59.4°, 62.0°, 72.3°, 76.1° and 76.4° 2θ degree angles. All the diffraction peaks of the as-synthesized max phase can be indexed to the Ti$_2$AlN reflections from JCPDS card no. 00-055-0434, which indicates the high purity of the as-synthesized Ti$_2$AlN MAX phase. This is consistent with previously reported XRD results [10,51]. The c-lattice parameter (c-LP) of the two-step annealed Ti$_2$AlN presented in Table 1 was calculated to be 13.59 Å using "unit cell" software from the XRD patterns explained in Figure 2a, and it closely matches with the reported Ti$_2$AlN c-LP value [21]. This is strong evidence of high purity of the as-synthesized MAX phase. For comparison, Ti$_2$AlN was also synthesized by a typical annealing process at 1100 °C without any step; its XRD pattern (red profile) is also shown in Figure 2a, which contains a prominent TiN peak at 42.6° and other impurities such as Ti$_2$Al$_5$ at 43.3° along with many unspecified peaks. This comparative study of the

XRD patterns clearly shows the improvement of the step annealing method over the normal annealing method. The FE-SEM image shown in Figure 2b depicts the layered compact structure, which is a typical signature of the MAX phases [4], confirming the successful synthesis of the 3D MAX phase using the unique step annealing method. Because the peak positions in the Raman spectra are correlated to the vibrational modes distinctive to a specific material, Raman spectroscopy is a powerful tool for identifying and characterizing the fingerprint of materials. The vibrational modes for the 211 MAX phases are theorized to be 24, but only four modes are Raman active and can be observed [52]. Of these four modes, ω_3 is infrared and Raman active, whereas the ω_4, ω_1, and ω_2 modes are only Raman active [52]. For the Ti_2AlN MAX phase, the ω_3 and ω_4 modes are associated with the parallel and perpendicular vibrations of the Ti-Ti planes, whereas the ω_1 and ω_2 vibrational modes arise from the shear vibrations of the Ti-Al planes [10,51,53]. The representative Raman spectra of step annealed Ti_2AlN are shown in Figure 2c, where all four Raman active modes are clearly observed at the peak positions of 149 cm^{-1} (ω_1), 229 cm^{-1} (ω_2), 234 cm^{-1} (ω_3), and 365 cm^{-1} (ω_4), providing strong evidence for the formation of the Ti_2AlN MAX phase [10,51,54].
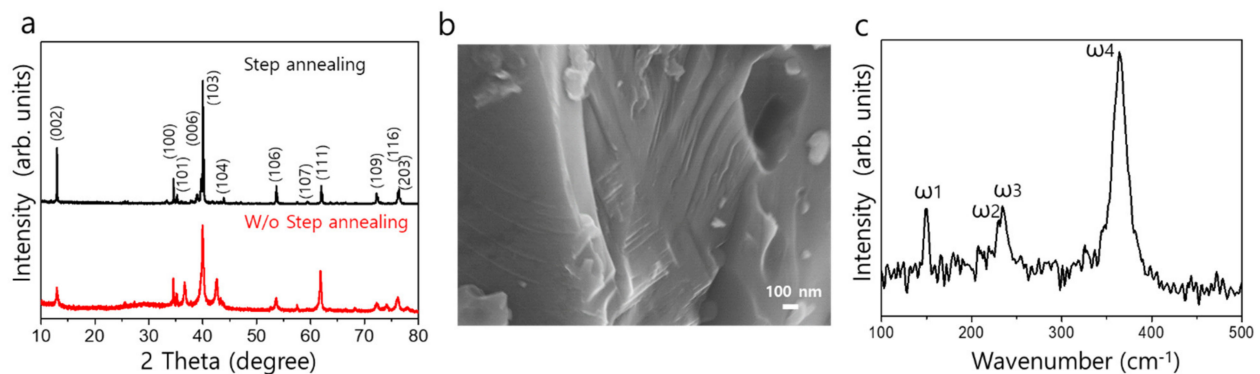

Figure 2. (**a**) XRD pattern, (**b**) FE–SEM image, and (**c**) Raman spectrum of as-synthesized Ti_2AlN MAX phase.

Table 1. Crystallographic details on structural determination of as-synthesized Ti_2AlN MAX phase.

Ti_2AlN	JCPDS-00-055-0434	As-Synthesized
Unit cell dimension (Å)	a = 2.989 c = 13.614	a = 2.995 c = 13.593
Cell volume (Å)^3	105.33	105.63

The step annealed Ti_2AlN MAX phase was further etched by wet chemical etching to obtain multilayered Ti_2N MXene sheets. In this particular method, the Al layer was removed by acid-salt treatment of the Ti_2AlN MAX phase in a KF-HCl etchant solution [10,26,45,55]. The effective formation and phase composition of multilayered Ti_2N MXene sheets were analyzed using XRD, FE-SEM, and Raman spectroscopy respectively, and the corresponding results are demonstrated in Figure 3. The prominent peaks observed in the XRD pattern were consistent with previously reported results for Ti_2N MXene, and they were indexed according to the JCPDS card no. 00-017-0386 of Ti_2N, as shown in Figure 3a. Comparative analysis of the XRD patterns of the Ti_2AlN MAX phase and Ti_2N MXene shows that the sharp peak assigned to the (0 0 2) peak in the Ti_2AlN MAX phase completely disappeared, and a broad curve was observed at that position. This observation may have resulted from the removal of the Al layer between two consecutive Ti_2N MXene layers [26]. Similarly, the intense peak assigned to the (1 0 3) plane observed in the Ti_2AlN MAX phase was completely absent in the XRD pattern of Ti_2N MXene, which is significant evidence of the effective etching of the Al layer from the Ti_2AlN MAX

phase [10,26]. A new peak at approximately 54.4° marked with "*" in Figure 3a is observed, which is assigned to the XRD signal of the potassium fluoride (KF) residue [56], which was used along with HCl in the etchant. This may have remained in the exfoliated Ti_2N MXene layers during the washing process. The formation of Ti_2N MXene was further confirmed by FE-SEM. The FE-SEM image in Figure 3b shows the typical morphological characteristics of MXenes [55,57,58]. The etched Ti_2N MXene showed visible delamination and increased space between the layers owing to the removal of the Al layer. In some areas, stacked layers appear instead of the delaminated and opened layers. This may be attributed to the intercalation of K^+ or water ions between the Ti_2N layers during the etching process. The presence of only two vibration modes at 222 cm^{-1} (ω_3) and 355 cm^{-1} (ω_4) confirms the formation of Ti_2N MXene sheets after etching the Al layer from the Ti_2AlN MAX phase observed in the Raman spectrum shown in Figure 3c. Comparative analysis of the Raman spectra of the Ti_2AlN MAX phase and the as-synthesized Ti_2N MXene sheets shows that the Ti-Al vibration mode (ω_1) is completely absent in the case of the Ti_2N MXene sheets, indicating the complete removal of the Al layer and formation of the Ti_2N MXene structure. Simultaneously, a clear red shift in the peak positions of ω_3 and ω_4 was observed for the Ti_2N MXene sheets compared to its parent MAX phase, clearly showing better etching of the Al layer along with exfoliation [10].
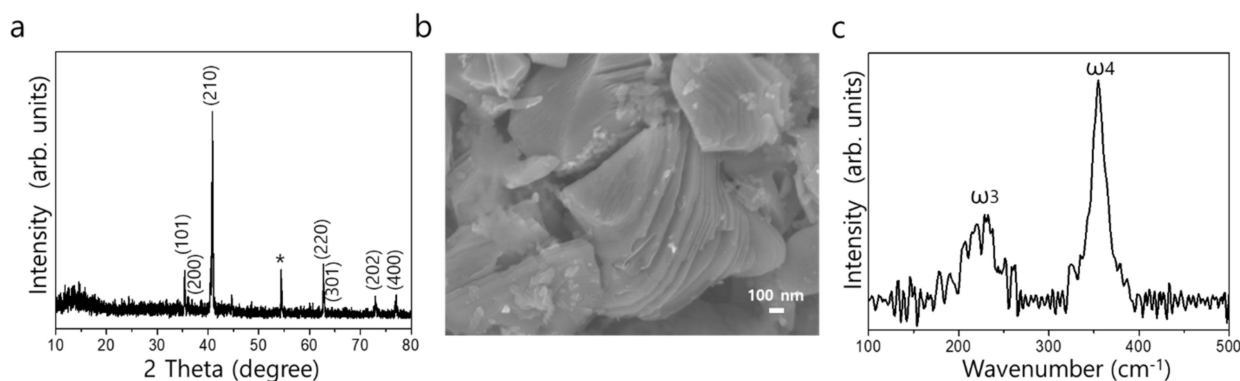

Figure 3. (**a**) XRD pattern, (**b**) FE–SEM image, (**c**) Raman spectrum of the layered Ti_2N MXene sheets.

The exfoliated Ti_2N MXene sheets were further decomposed into 0D Ti_2N MQDs using a simple hydrothermal method similar to the synthesis of QDs of other 2D materials, such as graphene and TMDs [30,59,60]. The effective synthesis of Ti_2N MQDs is based on two crucial steps: first, the Al layer is etched from the 3D Ti_2AlN MAX phase to obtain 2D Ti_2N MXene, and second, the MXene nanosheets are broken down into ultra-small Ti_2N MQDs, which determines the quality of the MQDs [26]. Since MXene is metastable it may yield its oxidation products in alkaline medium at high temperature reaction system. However, we emphasize that the hydrothermal reaction process at 100 °C using NH_4OH solution was adopted for the synthesis of MQDs where surface-terminated -NH groups from the NH_4OH solution maintain the crystal structure of pristine MXene, preventing the formation of TiO_2 or TiO_2 quantum dots [35]. The morphology and size of the Ti_2N MQDs were analyzed by HR-TEM and are presented in Figure 4a,b, respectively. The low-and high-magnification HR-TEM images in Figure 4a,b reveal the formation of uniform and ultra-small Ti_2N MQDs, respectively. The fringes observed in the single MQD in the HR-TEM image presented in Figure 4b are highly parallel with separation distance of 0.26 nm that corresponds to (1 0 1) lattice space of the Ti_2N [26] and reveal good crystallization of the Ti_2N MQDs. The fast Fourier transform (FFT) pattern of the MQDs is shown in the inset of Figure 4b. The average lateral diameter of the Ti_2N MQDs was determined to be 3.2 ± 0.2 nm from the bell-shaped size distribution curve, as shown in Figure 4c, which matches the size of the single MQD shown in Figure 4b. The element distribution was measured by XPS and the content of nitrogen in the MQDs was approximately 17.6%, which is comparable with the previously reported value of Ti_2N MXene [10].
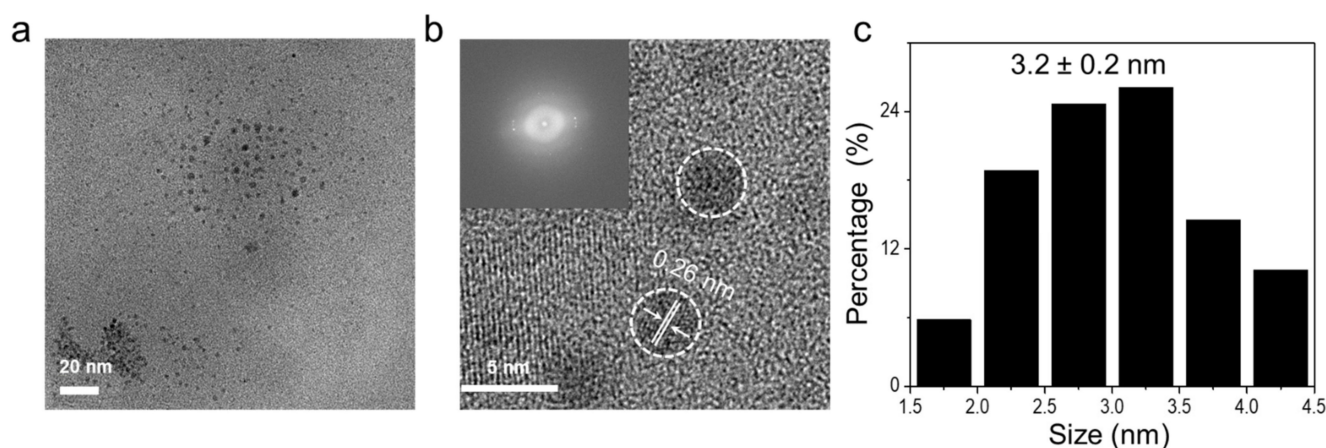
Figure 4. HR–TEM images (**a**) low, (**b**) high magnification, inset FFT image and (**c**) size distribution curve of the synthesized Ti$_2$N MQDs.

To study and understand the optical properties of the as-synthesized Ti$_2$N MQDs, absorption, PLE, and PL spectra were acquired from aqueous Ti$_2$N MQDs, and the results are presented in Figure 5. As-synthesized Ti$_2$N MQDs exhibited the PL emission with the peak wavelength around at 420 nm upon the excitation wavelength between 390 nm to 230 nm (Figure 5c). The demonstration of PL behavior indicated the successful fabrication of light emitting Ti$_2$N MQDs. The light emitting properties were observable due to quantum confinement effect which caused the bandgap expansion of semi-metal MXene that were previously observed from the fabrication of other MQDs and 2D material-derived QDs [26,33,35,46,60,61]. PLE spectrum is the plot of PL intensity at a fixed detection wavelength vs. the excitation wavelength. Because PLE intensity corresponds to the probability of optical transition, PLE spectra resemble the absorption spectra but with higher signal-to-noise ratio [62]. In our case, we performed PLE measurements to understand the correlation between PLE with PL and UV-vis absorption spectra. The measurement was done by fixing the detection wavelength of 410 ± 10 nm with varying excitation wavelengths ranging 225–400 nm. As shown in Figure 5a (black curve), the PLE spectrum displayed the two distinct peaks at 233 nm and 310 nm, which were consistent with the two absorption edges of the absorption spectrum (blue curve) [63]. The PLQY of 3 μM concentration of R6G solution in methanol has been found to be ~100% under visible excitation and can be used as the reference material to estimate the PLQY of other emissive materials [64]. The PLQY of MQDs was estimated using the following equation [65], which is presented in Figure 5b.

$$\Phi_{MQDs} = \Phi_{Ref} \, \frac{I^{PL}_{MQDs}/A_{MQDs}}{I^{PL}_{Ref}/A_{Ref}} \tag{1}$$

Here, Φ_{MQDs} is the QY of the MQDs to be measured, Φ_{Ref} is the QY of the reference, I^{PL}_{MQDs} represents the PL intensity of the MQDs, I^{PL}_{Ref} represents the PL intensity of the reference, A_{MQDs} is the absorption of the MQDs, and A_{Ref} is the absorption of the reference.

The maximum PLQY was estimated to be ~6.9% with 310 nm excitation, which is consistent with the PLE and PL results presented in Figure 5a. Furthermore, excitation wavelength (within UV, ranging from 230 nm to 390 nm) dependent PL spectra were obtained, which are broad in shape owing to the inhomogeneous size distribution of MQDs in aqueous solution [61,66], as shown in Figure 5c. Red shifts in the PL peak positions along with a decrease in intensity were observed for the excitation wavelengths from 310 nm to 390 nm, which may be due to the various sizes of the MQDs dispersed in the aqueous medium. Under the higher wavelength (lower energy) excitation, the small MQDs with a large band gap will be less excited, resulting in a lesser intensity due to the loss of emission at short wavelengths along with red-shifted peak positions and vice-versa. Remarkably,

we observed a high intensity of the emission under excitation at ~ 230 nm and 310 nm, which may be due to most of the MQDs being excited under this illumination. This is quite consistent with our absorption, PLE, and PLQY results shown in Figure 5a,b.
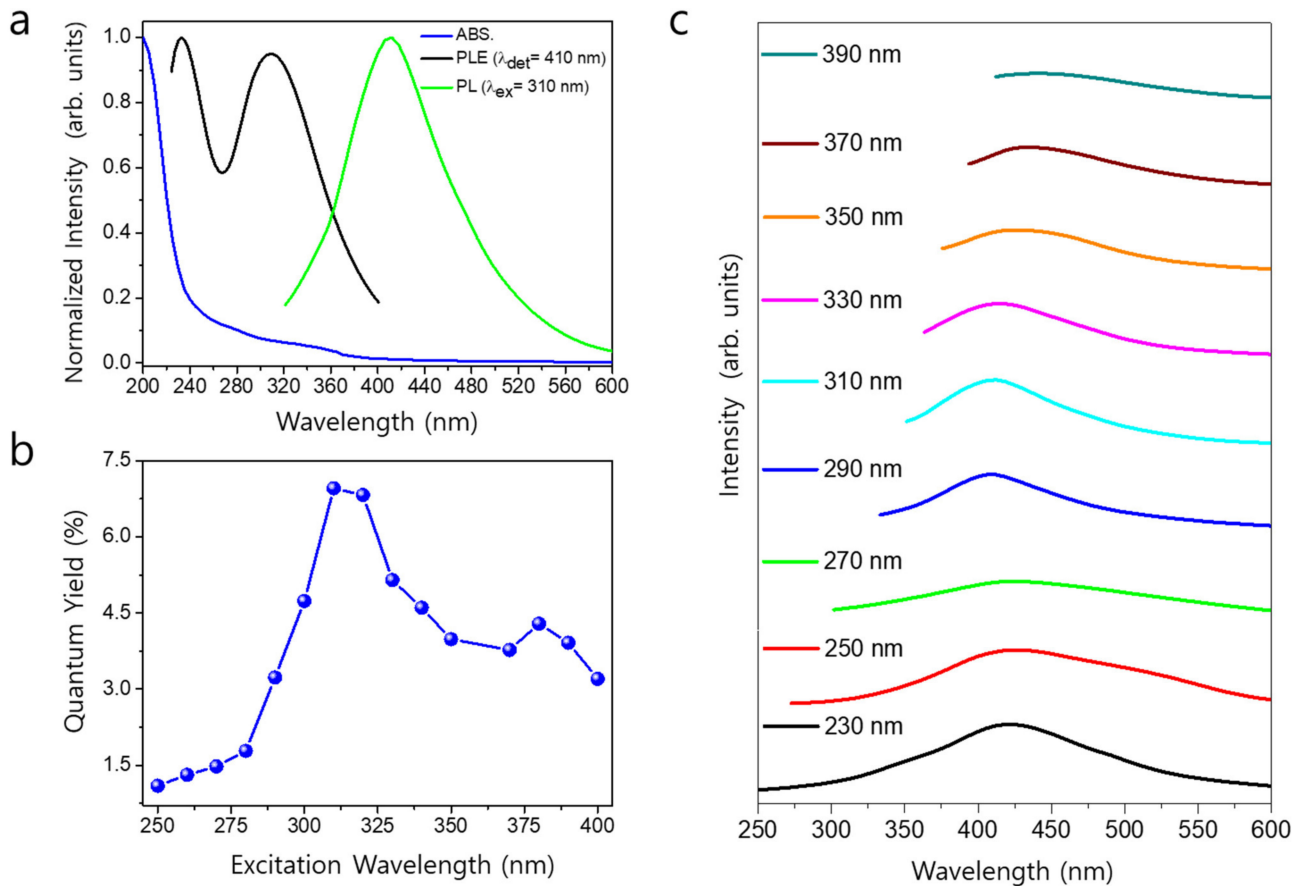

Figure 5. (**a**) UV-visible, PLE and PL spectra. Excitation wavelength dependent (**b**) PLQY and (**c**) PL spectra of the synthesized Ti_2N MQDs.

4. Conclusions

The Ti_2AlN MAX phase was prepared by two-steps annealing method at a significantly lower temperature than that used in previous methods. Furthermore, 2D MXene and MQDs were obtained that displayed efficient PL upon UV light absorption. The facile method of light emitting MQDs reported here will help expand the use of MXene and MQDs in nanophotonic applications.

References

1. Joelsson, T.; Hörling, A.; Birch, J.; Hultman, J. Single-crystal Ti_2AlN thin films. *Appl. Phys. Lett.* **2005**, *86*, 111913. [CrossRef]
2. Liu, W.; Qiu, C.; Zhou, J.; Ding, Z.; Zhou, X.; Du, S.; Han, Y.H.; Huang, Q. Fabrication of Ti_2AlN ceramics with orientation growth behavior by the microwave sintering method. *J. Eur. Ceram. Soc.* **2015**, *35*, 1385–1391. [CrossRef]
3. Li, M.; Lu, J.; Luo, k.; Li, Y.; Chang, K.; Chen, K.; Zhou, J.; Rosen, J.; Hultman, L.; Eklund, P.; et al. Element Replacement Approach by Reaction with Lewis Acidic Molten Salts to Synthesize Nanolaminated MAX Phases and MXenes. *J. Am. Chem. Soc.* **2019**, *141*, 4730–4737. [CrossRef]
4. Salvo, C.; Chicardi, E.; Poyato, R.; García-Garrido, C.; Jiménez, J.A.; López-Pernía, C.; Tobosque, P.; Mangalaraja, R.V. Synthesis and characterization of a nearly single bulk Ti_2AlN max phase obtained from Ti/AlN powder mixture through spark plasma sintering. *Materials* **2021**, *14*, 2217. [CrossRef] [PubMed]
5. Sokol, M.; Natu, V.; Kota, S.; Barsoum, M.W. On the Chemical Diversity of the MAX Phases. *Trends Chem.* **2019**, *1*, 210–223. [CrossRef]
6. Li, X.; Gonzalez-Julian, J.; Malzbender, J. Fabrication and mechanical performance of Ti_2AlN prepared by FAST/SPS. *J. Eur. Ceram. Soc.* **2020**, *40*, 4445–4453. [CrossRef]
7. Wang, X.H.; Zhou, Y.C. Layered Machinable and Electrically Conductive Ti_2AlC and Ti_3AlC_2 Ceramics: A Review. *J. Mater. Sci. Technol.* **2010**, *26*, 385–416. [CrossRef]
8. Sun, Z.; Music, D.; Ahuja, R.; Schneider, J.M. Ab initio study of M_2AlN (M = Ti, V, Cr). *J. Phys. Condens. Matter.* **2005**, *17*, L15–L19. [CrossRef]
9. Gao, J.; Li, C.; Wang, N.; Du, Z. Thermodynamic analysis of the Ti-Al-N system. *J. Univ. Sci. Technol. Beijing* **2008**, *15*, 420–424. [CrossRef]
10. Soundiraraju, B.; George, B.K. Two-Dimensional Titanium Nitride (Ti_2N) MXene: Synthesis, Characterization, and Potential Application as Surface-Enhanced Raman Scattering Substrate. *ACS Nano* **2017**, *11*, 8892–8900. [CrossRef]
11. Din, M.F.U.; Yang, C.; Tang, Y.; Tian, Y.; Luo, Y.; Wu, Y.; Que, W. Efficient and cost-effective method to synthesize highly purified Ti_4AlN_3 and Ti_2AlN. *J. Adv. Dielectr.* **2019**, *9*, 1950008. [CrossRef]
12. Kovalev, D.Y.; Luginina, M.A.; Sytschev, A.E. Reaction synthesis of the Ti_2AlN MAX-phase. *Russ. J. Non-Ferrous Met.* **2017**, *58*, 303–307. [CrossRef]
13. Kondakov, A.A.; Studenikin, I.A.; Linde, A.V.; Kondakova, N.A.; Grachev, V.V. Synthesis of Ti_2AlN MAX-phase by sintering in vacuum. *IOP Conf. Ser. Mater. Sci. Eng.* **2019**, *558*, 012017. [CrossRef]
14. Ding, H.; Li, Y.; Lu, J.; Chen, K.; Li, M.; Persson, P.O.A.; Hultman, L.; Eklund, P.; Du, S.; Huang, Z.; et al. Synthesis of MAX phases Nb_2CuC and $Ti_2(Al_{0.1}Cu_{0.9})N$ by A-site replacement reaction in molten salts. *Mater. Res. Lett.* **2019**, *7*, 510–516. [CrossRef]
15. Roy, C.; Banerjee, P.; Bhattacharyya, S. Molten salt shielded synthesis (MS^3) of Ti_2AlN and V_2AlC MAX phase powders in open air. *J. Eur. Ceram. Soc.* **2020**, *40*, 923–929. [CrossRef]
16. Dash, A.; Vaßen, R.; Guillon, O.; Gonzalez-Julian, J. Molten salt shielded synthesis of oxidation prone materials in air. *Nat. Mater.* **2019**, *18*, 465–470. [CrossRef]
17. Scabarozi, T.; Ganguly, A.; Hettinger, J.D.; Loflan, S.E.; Amini, S.; Finkel, P.; El-Raghy, T.; Barsoum, M.W. Electronic and thermal properties of $Ti_3Al(C_{0.5},N_{0.5})_2$, $Ti_2Al(C_{0.5},N_{0.5})$ and Ti_2AlN. *J. Appl. Phys.* **2008**, *104*, 073713. [CrossRef]
18. Gonzalez-Julian, J. Processing of MAX phases: From synthesis to applications. *J. Am. Ceram. Soc.* **2021**, *104*, 659–690. [CrossRef]
19. Barsoum, M.W.; Ali, M.; El-Raghy, T. Processing and characterization of Ti_2AlC, Ti_2AlN, and $Ti_2AlC_{0.5}N_{0.5}$. *Metall. Mater. Trans. A* **2000**, *31*, 1857–1865. [CrossRef]
20. Lane, N.J.; Vogel, S.C.; Barsoum, M.W. Temperature-dependent crystal structures of Ti_2AlN and Cr_2GeC as determined from high temperature neutron diffraction. *J. Am. Ceram. Soc.* **2011**, *94*, 3473–3479. [CrossRef]
21. Lin, Z.J.; Zhuo, M.J.; Li, M.S.; Wang, J.Y.; Zhou, Y.C. Synthesis and microstructure of layered-ternary Ti_2AlN ceramic. *Scr. Mater.* **2007**, *56*, 1115–1118. [CrossRef]
22. Ming, Y.; Yan-lin, C.; Bing-chu, M.; Jiao-qun, Z. Synthesis of high-purity Ti_2AlN ceramic by hot pressing. *Trans. Nonferrous Met. Soc. China* **2008**, *18*, 82–85.
23. Lyu, J.; Kashkarov, E.B.; Travitzky, N.; Syrtanov, M.S.; Lider, A.M. Sintering of MAX-phase materials by spark plasma and other methods. *J. Mater. Sci.* **2021**, *56*, 1980–2015. [CrossRef]
24. Cui, B.; Sa, R.; Jayaseelan, D.D.; Inam, F.; Reece, M.J.; Lee, W.E. Microstructural evolution during high-temperature oxidation of spark plasma sintered Ti_2AlN ceramics. *Acta Mater.* **2012**, *60*, 1079–1092. [CrossRef]
25. Jordan, J.L.; Thadhani, N.N. Effect of Shock-Activation on Post-shock Reaction Synthesis of Ternary Ceramics. *AIP Conf. Proc.* **2002**, *620*, 1097–1100.
26. Shao, J.; Zhang, J.; Jiang, C.; Lin, J.; Huang, P. Biodegradable titanium nitride MXene quantum dots for cancer phototheranostics in NIR-I/II biowindows. *Chem. Eng. J.* **2020**, *400*, 126009. [CrossRef]
27. Chung, S.; Revia, R.A.; Zhang, M. Graphene Quantum Dots and Their Applications in Bioimaging, Biosensing, and Therapy. *Adv. Mater.* **2021**, *33*, 1904362. [CrossRef]
28. Ding, X.; Peng, F.; Zhou, J.; Gong, W.; Slaven, G.; Loh, K.P.; Lim, C.T.; Leong, D.T. Defect engineered bioactive transition metals dichalcogenides quantum dots. *Nat. Commun.* **2019**, *10*, 41. [CrossRef]
29. Xu, Y.; Yan, L.; Li, X.; Xu, H. Fabrication of transition metal dichalcogenides quantum dots based on femtosecond laser ablation. *Sci. Rep.* **2019**, *9*, 2931. [CrossRef]

30. Roy, S.; Neupane, G.P.; Dhakal, K.P.; Lee, J.B.; Yun, S.J.; Han, G.H.; Kim, J.K. Observation of charge transfer in heterostructures composed of MoSe$_2$ quantum dots and a monolayer of MoS$_2$ or WSe$_2$. *J. Phys. Chem. C* **2017**, *121*, 1997–2007. [CrossRef]

31. Soleymaniha, M.; Shahbazi, M.A.; Rafieerad, A.R.; Maleki, A.; Amiri, A. Promoting Role of MXene Nanosheets in Biomedical Sciences: Therapeutic and Biosensing Innovations. *Adv. Healthc. Mater.* **2019**, *8*, 1801137. [CrossRef] [PubMed]

32. Naguib, M.; Mochalin, V.N.; Barsoum, M.W.; Gogotsi, Y. 25th anniversary article: MXenes: A new family of two-dimensional materials. *Adv. Mater.* **2014**, *26*, 992–1005. [CrossRef] [PubMed]

33. Yang, G.; Zhao, J.; Yi, S.; Wan, X.; Tang, J. Biodegradable and photostable Nb$_2$C MXene quantum dots as promising nanofluorophores for metal ions sensing and fluorescence imaging. *Sens. Actuators B Chem.* **2020**, *309*, 127735. [CrossRef]

34. Desai, M.L.; Basu, H.; Singhal, R.K.; Saha, S.; Kailasa, S.K. Ultra-small two dimensional MXene nanosheets for selective and sensitive fluorescence detection of Ag$^+$ and Mn^{2+} ions. *Colloids Surf. A* **2019**, *565*, 70–77. [CrossRef]

35. Xue, Q.; Zhang, H.; Zhu, M.; Pei, Z.; Li, H.; Wang, Z.; Huang, Y.; Huang, Y.; Deng, Q.; Zhou, J.; et al. Photoluminescent Ti$_3$C$_2$ MXene Quantum Dots for Multicolor Cellular Imaging. *Adv. Mater.* **2017**, *29*, 1604847. [CrossRef] [PubMed]

36. Zhang, Q.; Sun, Y.; Liu, M.; Liu, Y. Selective detection of Fe^{3+} ions based on fluorescence MXene quantum dots via a mechanism integrating electron transfer and inner filter effect. *Nanoscale* **2020**, *12*, 1826–1832. [CrossRef]

37. Yong, K.-T.; Law, W.-C.; Hu, R.; Ye, L.; Liu, L.; Swihart, M.T.; Prasad, P.N. Nanotoxicity assessment of quantum dots: From cellular to primate studies. *Chem. Soc. Rev.* **2013**, *42*, 1236–1250. [CrossRef]

38. Hoshino, A.; Hanada, S.; Yamamoto, K. Toxicity of nanocrystal quantum dots: The relevance of surface modifications. *Arch. Toxicol.* **2011**, *85*, 707–720. [CrossRef]

39. Ai, F.; Fu, C.; Cheng, G.; Zhang, H.; Feng, Y.; Yan, X.; Zheng, X. Amino-Functionalized Ti$_3$C$_2$ MXene Quantum Dots as Photoluminescent Sensors for Diagnosing Histidine in Human Serum. *ACS Appl. Nano Mater.* **2021**, *4*, 8192–8199. [CrossRef]

40. Guan, Q.; Ma, J.; Yang, W.; Zhang, R.; Zhang, X.; Dong, X.; Fan, Y.; Cai, L.; Cao, Y.; Zhang, Y.; et al. Highly fluorescent Ti$_3$C$_2$ MXene quantum dots for macrophage labeling and Cu^{2+} ion sensing. *Nanoscale* **2019**, *11*, 14123–14133. [CrossRef]

41. Miao, S.; Chen, D.; Madani, A.; Jorgensen, M.R.; Bolaños Quiñones, V.A.; Ma, L.; Hickey, S.G.; Eychmüller, A.; Schmidt, O.G. Optofluidic Sensor: Evaporation Kinetics Detection of Solvents Dissolved with Cd$_3$P$_2$ Colloidal Quantum Dots in a Rolled-Up Microtube. *Ade. Opt. Mater.* **2015**, *3*, 187–193. [CrossRef]

42. Madani, A.; Ma, L.; Miao, S.; Jorgensen, M.R.; Schmidt, O.G. Luminescent nanoparticles embedded in TiO$_2$ microtube cavities for the activation of whispering-gallery-modes extending from the visible to the near infrared. *Nanoscale* **2016**, *8*, 9498–9503. [CrossRef] [PubMed]

43. Wang, C.; Chen, Q.; Chen, H.; Liu, J.; Song, Y.; Liu, J.; Li, D.; Ge, Y.; Gong, Y.; Zhang, Y.; et al. Boron quantum dots all-optical modulator based on efficient photothermal effect. *Opto-Electron. Adv.* **2021**, *4*, 200032. [CrossRef]

44. Yang, F.; Ge, Y.; Yin, T.; Guo, J.; Zhang, F.; Tang, X.; Qiu, M.; Liang, W.; Xu, N.; Wang, C.; et al. Ti$_3$C$_2$T$_x$ MXene Quantum Dots with Enhanced Stability for Ultrafast Photonics. *ACS Appl. Nano Mater.* **2020**, *3*, 11850–11860. [CrossRef]

45. Sharbirin, A.S.; Akhtar, S.; Kim, J.Y. Light-emitting MXene quantum dots. *Opto-Electron. Adv.* **2021**, *4*, 200077. [CrossRef]

46. Huang, D.; Xie, Y.; Lu, D.; Wang, Z.; Wang, J.; Yu, H.; Zhang, H. Demonstration of a White Laser with V$_2$C MXene-Based Quantum Dots. *Adv. Mater.* **2019**, *31*, 1901117. [CrossRef]

47. Venkatkarthick, R.; Rodthongkum, N.; Zhang, X.; Wang, S.; Pattananuwat, P.; Zhao, Y.; Liu, R.; Qin, J. Vanadium-Based Oxide on Two-Dimensional Vanadium Carbide MXene (V$_2$O$_x$@V$_2$CT$_x$) as Cathode for Rechargeable Aqueous Zinc-Ion Batteries. *ACS Appl. Energy Mater.* **2020**, *3*, 4677–4689. [CrossRef]

48. Salvo, C.; Chicardi, E.; García-Garrido, C.; Poyato, R.; Jiménez, J.A.; Mangalaraja, R.V. Study of the Influence of Sintering Atmosphere and Mechanical Activation on the Synthesis of Bulk Ti$_2$AlN MAX Phase Obtained by Spark Plasma Sintering. *Materials* **2021**, *14*, 4574. [CrossRef]

49. Tunca, B.; Lapauw, T.; Delville, R.; Neuville, D.R.; Hennet, L.; Thiaudière, D.; Ouisse, T.; Hadermann, J.; Vleugels, J.; Lambrinou, K. Synthesis and Characterization of Double Solid Solution (Zr,Ti)$_2$(Al,Sn)C MAX Phase Ceramics. *Inorg. Chem.* **2019**, *58*, 6669–6683. [CrossRef]

50. Wang, Z.; Liu, J.; Wang, L.; Li, X.; Ke, P.; Wang, A. Dense and high-stability Ti$_2$AlN MAX phase coatings prepared by the combined cathodic arc/sputter technique. *Appl. Surf. Sci.* **2017**, *396*, 1435–1442. [CrossRef]

51. Chen, W.; Tang, J.; Lin, X.; Ai, Y.; Ye, N. Formation mechanism of high-purity Ti$_2$AlN powders under microwave sintering. *Materials* **2020**, *13*, 5356. [CrossRef] [PubMed]

52. Presser, V.; Naguib, M.; Chaput, L.; Togo, A.; Hug, G.; Barsoum, M.W. First-order Raman scattering of the MAX phases: Ti$_2$AlN, Ti$_2$AlC$_{0.5}$N$_{0.5}$, Ti$_2$AlC, (Ti$_{0.5}$V$_{0.5}$)$_2$AlC, V$_2$AlC, Ti$_3$AlC$_2$, and Ti$_3$GeC$_2$. *J. Raman Spectrosc.* **2012**, *43*, 168–172. [CrossRef]

53. Spanier, J.E.; Gupta, S.; Amer, M.; Barsoum, M.W. Vibrational behavior of the M$_{n+1}$AX$_n$ phases from first-order Raman scattering (M = Ti, V, Cr, A = Si, X = C, N). *Phys. Rev. B* **2005**, *71*, 012103. [CrossRef]

54. Gröner, L.; Lutz, K.; Sabine, O.; Alexander, F.; Marco, W.; Frank, M.; Frank, B.; Chris, E. Microstructural investigations of polycrystalline Ti$_2$AlN prepared by physical vapor deposition of Ti-AlN multilayers. *Surf. Coat. Technol.* **2018**, *343*, 166–171. [CrossRef]

55. Szuplewska, A.; Rozmysłowska-Wojciechowska, A.; Poźniak, S.; Wojciechowski, T.; Birowska, M.; Popielski, M.; Chudy, M.; Ziemkowska, W.; Chlubny, L.; Moszczyńska, D.; et al. Multilayered stable 2D nano-sheets of Ti$_2$NT$_x$ MXene: Synthesis, characterization, and anticancer activity. *J. Nanobiotech.* **2019**, *17*, 114. [CrossRef]

56. Sandesh, S.; Shanbhag, G.V.; Halgeri, A.B. Transesterification of Glycerol to Glycerol Carbonate Using KF/Al$_2$O$_3$ Catalyst: The Role of Support and Basicity. *Catal. Lett.* **2013**, *143*, 1226–1234. [CrossRef]

57. Jastrzebska, A.M.; Karwoska, E.; Wojciechowski, T.; Ziemkowska, W.; Rozmyslowska, A.; Chlubny, L.; Olszyna, A. The Atomic Structure of Ti$_2$C and Ti$_3$C$_2$ MXenes is Responsible for Their Antibacterial Activity toward E. coli Bacteria. *J. Mater. Eng. Perform.* **2019**, *28*, 1272–1277. [CrossRef]

58. Rozmysłowska-Wojciechowska, A.; Wojciechowski, T.; Ziemkowska, W.; Chlubny, L.; Olszyna, A.; Jastrzębska, A.M. Surface interactions between 2D Ti$_3$C$_2$/Ti$_2$C MXenes and lysozyme. *Appl. Surf. Sci.* **2019**, *473*, 409–418. [CrossRef]

59. Liu, Y.; Zhou, Q.; Yuan, Y.; Wu, Y. Hydrothermal synthesis of fluorescent carbon dots from sodium citrate and polyacrylamide and their highly selective detection of lead and pyrophosphate. *Carbon* **2017**, *115*, 550–560. [CrossRef]

60. Huang, H.; Du, C.; Shi, H.; Feng, X.; Li, J.; Tan, Y.; Song, W. Water-Soluble Monolayer Molybdenum Disulfide Quantum Dots with Upconversion Fluorescence. *Part. Part. Syst. Charact.* **2015**, *32*, 72–79. [CrossRef]

61. Jin, H.; Baek, B.; Kim, D.; Wu, F.; Batteas, J.D.; Cheon, J.; Son, D.H. Effects of Direct Solvent-Quantum Dot Interaction on the Optical Properties of Colloidal Monolayer WS$_2$ Quantum Dots. *Nano Lett.* **2017**, *17*, 7471–7477. [CrossRef] [PubMed]

62. Brocke, T. *Electronic Raman Spectroscopy on Semiconductor Quantum Dots*; Cuvillier Verlag: Göttingen, Germany, 2007; pp. 15–17.

63. Sharbirin, A.S.; Roy, S.; Tran, T.T.; Akhtar, S.; Singh, J.; Duong, D.L.; Kim, J. Light-Emitting Ti$_2$N (MXene) Quantum Dots: Synthesis, Characterization and Theoritical Calculations. *J. Mater. Chem. C* **2022**. [CrossRef]

64. Magde, D.; Wong, R.; Seybold, P.G. Fluorescence Quantum Yields and Their Relation to Lifetimes of Rhodamine 6G and Fluorescein in Nine Solvents: Improved Absolute Standards for Quantum Yields. *Photochem. Photobiol.* **2002**, *75*, 327–334. [CrossRef]

65. Roy, S.; Sharbirin, A.S.; Lee, Y.; Kim, W.B.; Kim, T.S.; Cho, K.; Kang, K.; Jung, H.S.; Kim, J. Measurement of quantum yields of monolayer TMDs using dye-dispersed PMMA thin films. *Nanomaterials* **2020**, *10*, 1032. [CrossRef] [PubMed]

66. Pan, D.; Guo, L.; Zhang, J.; Xi, C.; Xue, Q.; Hunag, H.; Li, J.; Zhang, Z.; Yu, W.; Chen, z.; et al. Cutting sp^2 clusters in graphene sheets into colloidal graphene quantum dots with strong green fluorescence. *J. Mater. Chem.* **2012**, *22*, 3314–3318. [CrossRef]